J Mater Sci (2023) 58:3346–3359

Metals & corrosion

Preparation and properties of Fe–Mn–Si–Cr–Ni shape memory alloy

Qin Zou[1,2], Xihui Ye[2], Yanguo Li[1,*], Wenqi Luo[2], and Yongan Luo[1]

[1] *State Key Laboratory of Metastable Materials Science and Technology, Yanshan University, Qinhuangdao 066004, Hebei, China*
[2] *College of Mechanical Engineering, Yanshan University, Qinhuangdao 066004, Hebei, China*

Received: 28 October 2022
Accepted: 21 January 2023
Published online:
7 February 2023

© The Author(s), under exclusive licence to Springer Science+Business Media, LLC, part of Springer Nature 2023

ABSTRACT

Fe–Mn–Si–Cr–Ni shape memory alloys (SMAs) were prepared by mechanical alloying and discharge plasma sintering. The effects of milling time on the microstructure evolution, mechanical properties, superelasticity and corrosion resistance of Fe–Mn–Si–Cr–Ni SMAs (both powder and sintered bulks) were investigated. With the increase in milling time, the alloy powder gradually formed a solid solution with body-centered cubic (BCC) as the main phase. The increase in milling time promoted the phase transition (BCC → FCC + BCC2) during the sintering of the alloy, and the BCC2 content in the alloy sintered bulks increased with the increase in milling time. The higher the BCC2 content, the higher the yield strength, compressive strength and hardness of the alloy. The BCC2 phase affected the superelasticity of the alloy by changing the yield strength of the alloy, the higher the yield strength, the stronger the superelasticity of the alloy. The A2 alloy had the best superelasticity, with a superelastic strain of 2.8%. The A2 alloy had higher corrosion resistance in NaOH solution than in HCl solution.

Handling Editor: Catalin Croitoru.

Qin Zou, Xihui Ye and Yanguo Li have contributed equally to this paper.

Address correspondence to E-mail: lyg@ysu.edu.cn

https://doi.org/10.1007/s10853-023-08239-3

GRAPHICAL ABSTRACT

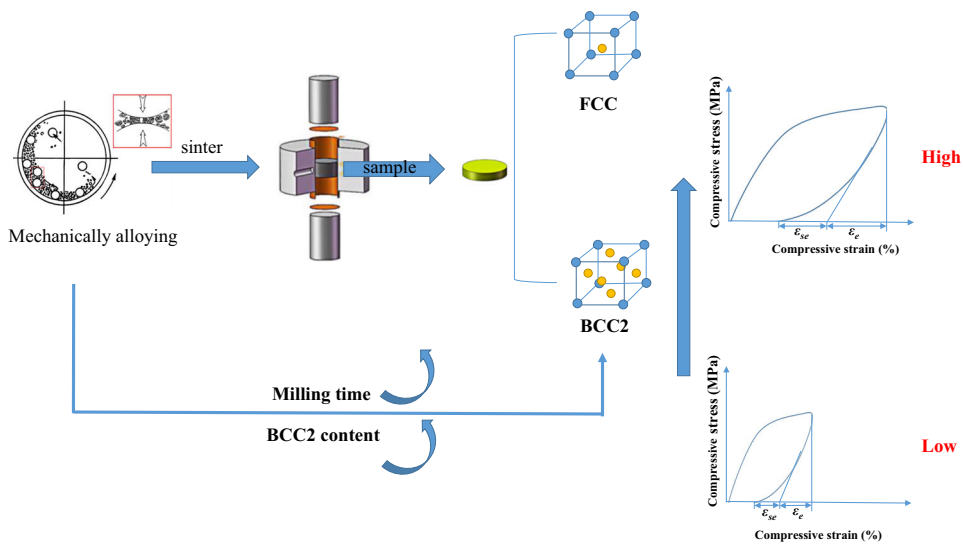

Introduction

The memory effect of Fe–Mn–Si-based alloy was realized by stress-induced martensitic transformation and its reverse transformation [1–3]. Under the action of stress, the alloy phase was transformed from face-centered cubic austenite (γ-FCC) to hexagonal dense martensite (ε-HCP). After unloading, ε-HCP was transformed into the γ-FCC phase at a temperature higher than A_f (austenite finish), and the effect of shape recovery was achieved [4]. Fe–Mn–Si-based shape memory alloy (SMA) had become one of the most likely shape memory alloys for large-scale industrial applications due to its low cost of raw materials, easy processing and manufacturing, and excellent mechanical properties. It was widely used in the manufacture of vibration pipe joints [5] and degradable biomaterials [6]. At present, the shape memory performance of Fe–Mn–Si-based SMAs could be improved by optimizing alloying elements and preparation methods.

Generally, Fe–Mn–Si-based shape memory alloys are produced by melting and casting in a high vacuum (or air) environment combined with thermal machining [7]. However, ingot metallurgy has some inherent defects, such as difficulty in maintaining the uniformity of alloy composition, easy loss of Mn element during heat treatment or melting, crack during solidification or quenching and incomplete dissolution of Si in the melt [8]. The study of A. Šalak with H. Danninger showed that compared with Fe–Mn–Si memory alloy prepared by vacuum melting, Fe–Mn–Si memory alloy prepared by powder metallurgy (P/M) solves the shortcoming of incomplete solution of Mn and Si elements [9, 10]. Compared with the traditional hot pressing sintering and hot isostatic pressing sintering methods, the spark plasma sintering (SPS) method can solidify the alloy powder and form a high-density structure with finer grains at a relatively lower temperature and in a shorter time [11–13]. The densities of Fe–Mn–Si memory alloys prepared by Z.G. Xu [6, 14] using hot pressing sintering were 62.8% and 67.6%, respectively. In contrast, the densities of Fe–Mn–Si memory alloys prepared by Spandana D [15] using the SPS method reached 98%. There are usually two ways to prepare alloys via P/M. One involves mixing powders of various alloying elements and then sintering them. The other is to mechanically alloying (MA) the powder and then sintered. MA can effectively reduce the particle size of the powder mixture [16–19], making the alloy powder synthesize saturated solid solution preferably [20], promoting the diffusion and phase transformation of elements in subsequent

sintering, which is beneficial to the shape recovery performance of the alloy. At the same time, MA can increase the hardness and compressive strength of the alloy [21, 22]. Z.G. Xu [14] found that the alloy sintered with MA has a compressive strength of 454.5 MPa, which is 190% higher than that of the alloy sintered without MA under the same conditions. In the Fe–Mn–Si SMA prepared by Takeshi Saito [23] using MA combined with SPS sintering process, the compressive strength of the alloy is as high as 950 MPa when the compressive strain is 0.08. Therefore, it is highly necessary to perform MA on the alloy powder before sintering. However, in MA, the milling medium, rotational speed, milling time, ball–powder weight ratio and milling atmosphere all affect the microstructure and properties of the alloy powders [24–27]. The hardness of Fe–17Mn–6Si–0.03C alloy prepared by F. Xu [28] using MA for 20 min was only 130 HV, while the hardness of He–Mn–Si-based alloy prepared by Zou et al. [29] using MA for 50 h was as high as 527.4 HV.

In this work, the Fe–Mn–Si–Cr–Ni alloy was by MA combined with SPS. The effect of milling time on the microstructure, mechanical properties, superelasticity and corrosion resistance of the alloy had been investigated.

Experimental details

High-purity (99.9 wt.%) Fe, Mn, Si, Cr and Ni powders were mixed according to the mass ratio (61Fe–20Mn–6Si–8Cr–5Ni) required for the experiment. The alloy powder was mechanically alloyed with a planetary ball mill (QM-3SP4, China) (400 r/min, argon atmosphere, grinding time: 50 h, ball–material weight ratio: 20:1). Both the grinding media and the grinding vessel were made of stainless steel, and methanol was used as a control agent during milling. To avoid excessive cold welding, ramming was performed every 10 h. The alloy powder was sintered into Φ10 alloy bulks using SPS equipment (Labox-110, Japan) [15], and the sintering parameters were 950 °C /50 MPa/30 min/50 °C·min^{-1}.

An X-ray diffractometer (D/MAX-2500PC, Rigaku, Japan) was used to analyze the phase structure of the alloy. An FE-S-4800 field emission scanning electron microscope was used to observe the microstructure of the surface and fracture of the sintered samples, and energy dispersion spectroscopy (EDS) was used to analyze the chemical composition of the microzone. DSC analysis of alloy powder was carried out by a differential scanning thermal analyzer (NETZSCH STA449C) (1300 °C/10 K/min/argon). At the same time, the Archimedes drainage method was used to measure the relative density of samples ($\eta = \rho_0/\rho_1$, where η is the relative density of the sample, ρ_0 is the actual density of the sample and ρ_1 is the theoretical density of the sample). The sintered samples were polished and placed into a Vickers hardness tester (HVS-1000) to test the hardness of the samples. A dynamic thermo-mechanical simulation machine (Gleeble-3500) was used to test the sample's compressive mechanical properties and superelastic strain (Φ4 mm × 8 mm cylinder) at room temperature. The corrosion resistance of the alloy sample (8 mm × 8 mm × 6 mm) in 3%HCl and 20%NaOH solution was tested by static immersion weight loss method.

Results

As shown in Fig. 1a, XRD patterns of alloy powders with different milling times show that the diffraction peaks of Fe, Mn, Si, Cr, and Ni significantly decrease or disappear with the increase in milling time, and elements Mn, Si, Cr, and Ni are solubly dissolved into α-Fe. Because the integrity of the crystal is destroyed by milling, the intensity of the diffraction peak decreases. In the subsequent milling stage, the powders and the steel balls collide violently under external forces, which leads to an increase in stress between the powder particles and a gradual accumulation of defects. At about 50 h, the energy generated by MA transforms part of the lattice from the high-strain α-BCC phase to the ε-HCP phase, and the peak point of HCP increases gradually with the increase in milling time. The local relaxation caused by lattice distortion has little effect on the crystallite size variation, and the residual plastic strain can be neglected [30]. Therefore, the average crystallite size and lattice strain can be directly estimated by the Scherrer formula (1) and William–Hall formula (2), and the results are shown in Fig. 1b. The microcrystal size decreases from 261 to 79 nm within 0–10 h of milling, and the reduction in microcrystal size at this stage is mainly attributed to mechanical milling. In the subsequent milling process, the particle size decreases slowly, and the crystallite size gradually

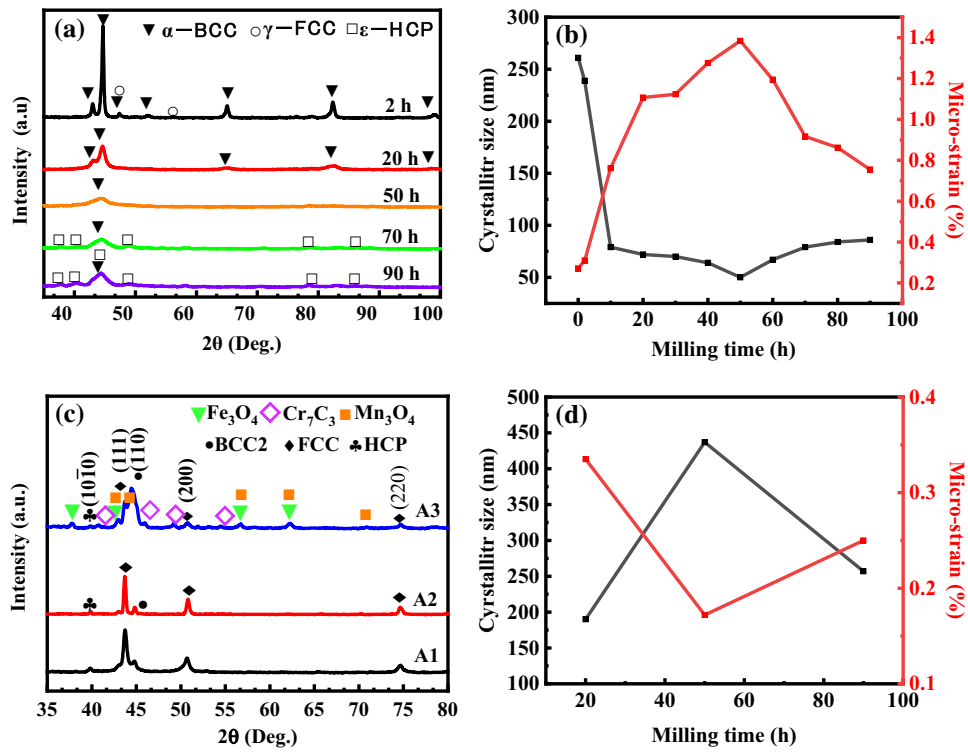

Figure 1 XRD patterns of Fe–20 Mn–6Si–8Cr–5Ni alloy powder and bulk at different milling times: **a**, **b** alloy powder; **c**, **b** alloy bulks.

stabilizes at about 70 nm. At 50 h, the particle size has a trough up to 50 nm. After 50 h, the cold welding makes part of the broken powder particles sticky, increasing the average crystallite size. The effect of the milling time on the lattice microstrain and the crystallite size of the alloy powder is the opposite. At the initial stage of milling, the lattice microstrain increases sharply, peaking at 50 h, and then shows a downward trend. Before 50 h, the lattice microstrain of the alloy powder is mainly associated with the formation of solid solutions in the powder. When the crystallite size is reduced to the nanometer scale, the volume fraction of the grain boundaries is large. The large amount of energy accumulated during milling causes other alloying elements to quickly dissolve into the main lattice, resulting in a large number of defects and severe lattice distortions. After 50 h, the fragmentation of the powder particles is in dynamical equilibrium with the cold welding process. The energy generated in the MA process will transform part of the high-strain α-BCC phase into the low-strain ε-HCP phase, resulting in the decrease in lattice microstrain.

$$a_{hkl} = \frac{k\lambda}{\beta \cos\theta} \tag{1}$$

$$\frac{\beta \cos\theta}{\lambda} = \frac{2\varepsilon \sin\theta}{\lambda} + \frac{\beta}{d} \tag{2}$$

where α_{hkl} is the crystallite size (nm) of different crystal planes, ε is the lattice microstrain (%), β is the half-height width of the diffraction peak of the test sample (°), λ is the wavelength of incident X-ray (λ = 1.54056A) and θ is the diffraction angle of different crystal planes.

The mechanical alloyed Fe–20Mn–6Si–8Cr–5Ni alloy powder was sintered at 950 °C to obtain the alloy bulks. The A1, A2 and A3 alloys were milled for 20 h, 50 h and 90 h, respectively. It can be found from Fig. 1c that the main phase of the alloy block before 50 h milling is the FCC phase. After 90 h of milling, the main phase changes to the BCC2 phase, and Fe_3O_4, Mn_3O_4 and $C_{r7}C_3$ also appear. The reason is that during the long MA process, the energy of the alloy powder is highly concentrated, which increases the activity of some elements in the alloy powder, and some elements are easy to combine with O and C in the air. It is found that with increasing milling time, the average crystallite size of the alloy first increases and then decreases, and the lattice strain first decreases and then increases. This result is in contrast to the trend of the lattice strain of alloy powders with milling time.

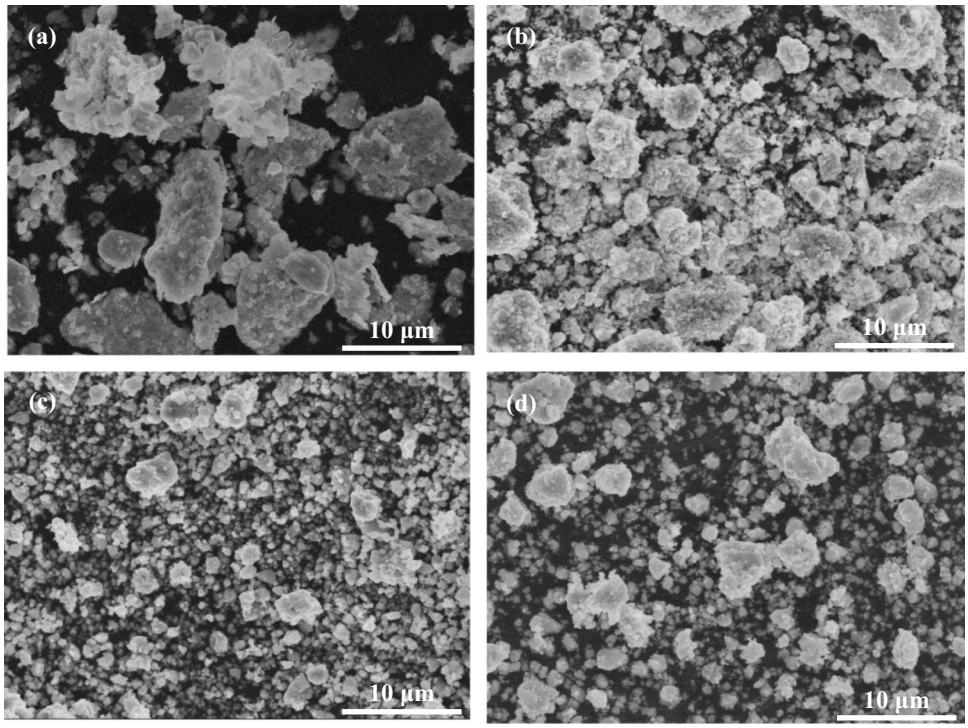

Figure 2 SEM images of alloy powders at different milling times: **a** 2 h, **b** 20 h, **c** 50 h, **d** 90 h.

In the early stage of milling in Fig. 2a, the elemental powders were simply mixed, and the small particles adhered to the large ones, forming particles with an average size of 10 μm. After 20 h, the particle size reached 5 μm, and the powder was solubilized. After 50 h of milling, large stresses are generated between the powders and defects gradually accumulate, resulting in microscopic cracks in the powder particles. Under the action of work hardening, the powder particles become brittle and the average particle size decreases further. At this stage, due to the balance between cold welding and fracture, the particle morphology tends to be hemispherical (Fig. 2c). After that, when the energy inside the powder accumulates continuously and reaches a certain value, the amorphous phase starts to be produced and the amorphous powder is gradually formed. In the final stage of milling, due to the mechanical crystallization of the amorphous phase, cold welding has a great impact on the powder, which increases the ductility of the powder and leads to the formation of irregularly shaped particles (Fig. 2d). From the powder element distribution diagram of Fe–20Mn–6Si–8Cr–5Ni alloy (Fig. 3), it was found that the powder elements of the alloy after milling for 20 h and 50 h were evenly distributed without obvious agglomeration, indicating that the chemical distribution was uniform. The alloy powder after milling for 20 h has a significantly higher amount of Fe and a lower amount of other elements than the nominal composition, indicating that the alloy powder is not fully soluble under these conditions. For milling times longer than 50 h, the elemental composition of each particle essentially reaches the nominal composition ratio.

The alloy prepared under the conditions of three different milling times had different microscopic morphologies (Fig. 4). Combining the EDS spot scan region analysis in Table 1, it can be seen that the white matrix phase is the FCC phase and the dark gray second phase is the BCC2 phase rich in Mn and Si. The BCC2 phase in the A1 alloy is approximately circular and uniformly distributed on the matrix. The BCC2 phase in the A2 alloy has an irregular shape and is significantly more abundant than in the A1 alloy. The distribution of the FCC phase in the A3 alloy is clearly reduced and divided by the BCC2 phase, showing a discontinuous distribution. Pores have also been found in the A3 alloy. The A1 and A2 alloys are typically continuous matrices surrounded by another phase structure. Since the matrix is a continuous FCC structure, the alloy has better plastic deformability and can exhibit better mechanical properties. By comparison, it can be found that alloys

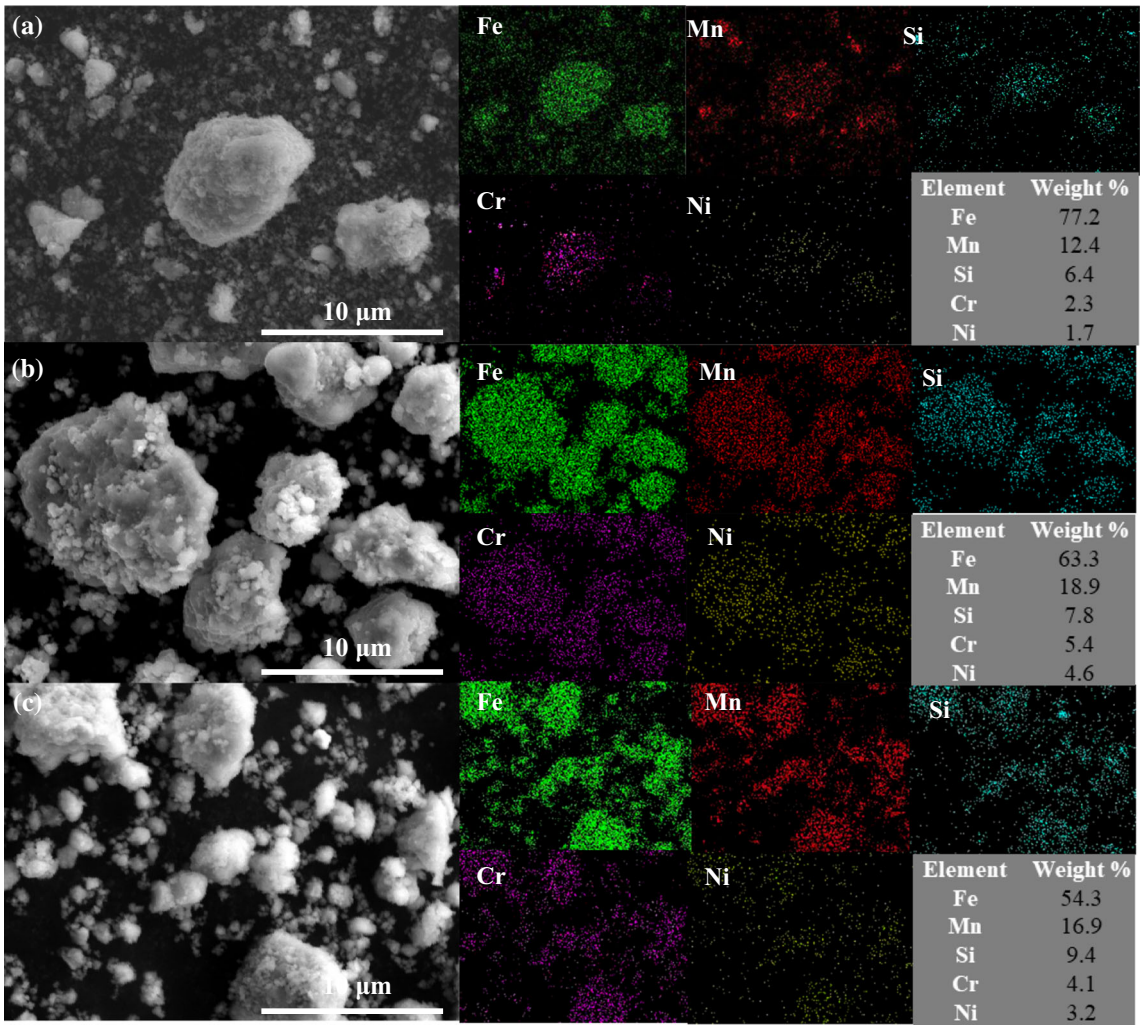

Figure 3 Mapping scan images of alloy powder surface: **a** 20 h, **b** 50 h, **c** 90 h.

A1 and A2 are completely dense and do not have significant pores.

The elementary content analysis of the EDS point sweep of the two phases in Fig. 4 is given in Table 1. The white phase (Point 1) in the A1 and A2 alloys basically conforms to the nominal composition, which is the FCC phase. The content of each element in the FCC phase of the A1 alloy deviates from the nominal composition compared to the A2 alloy, and the Cr content in the BCC2 phase is significantly higher. This is due to the incomplete solid solution of the alloy powder at 20 h of milling, which further confirms the results in Fig. 3. In the A3 alloy, there are large amounts of C and O elements, and Mn is more severely volatilized. Because the activity of each element increases after a long time of milling, the alloy powder is prone to volatilization and oxidation in the subsequent sintering [31].

According to Fig. 5, with the increase in temperature, exothermic peaks appear in the alloy powder at about 400 °C and 700 °C, and endothermic peaks appear at 900 °C, which indicates that the alloy powder has undergone phase transformation at these three temperatures.

The room-temperature compressive stress–strain curves for the A1, A2 and A3 alloys are shown in Fig. 6. The yield and fracture strength of the A1 alloy is 1143 MPa and 1450 MPa, respectively. The yield and fracture strength of the A2 alloy reaches their maximum values of 1326 MPa and 1753 MPa, respectively. The A3 alloy has a brittle fracture with a fracture strength of 1555 MPa as shown in Fig. 6. As the milling time increases, the compression rate of the alloy decreases from 24.1 to 5.6%, but the hardness of the alloy gradually increases, as shown in Table 2. The relative densities of the A1, A2 and A3 alloys are

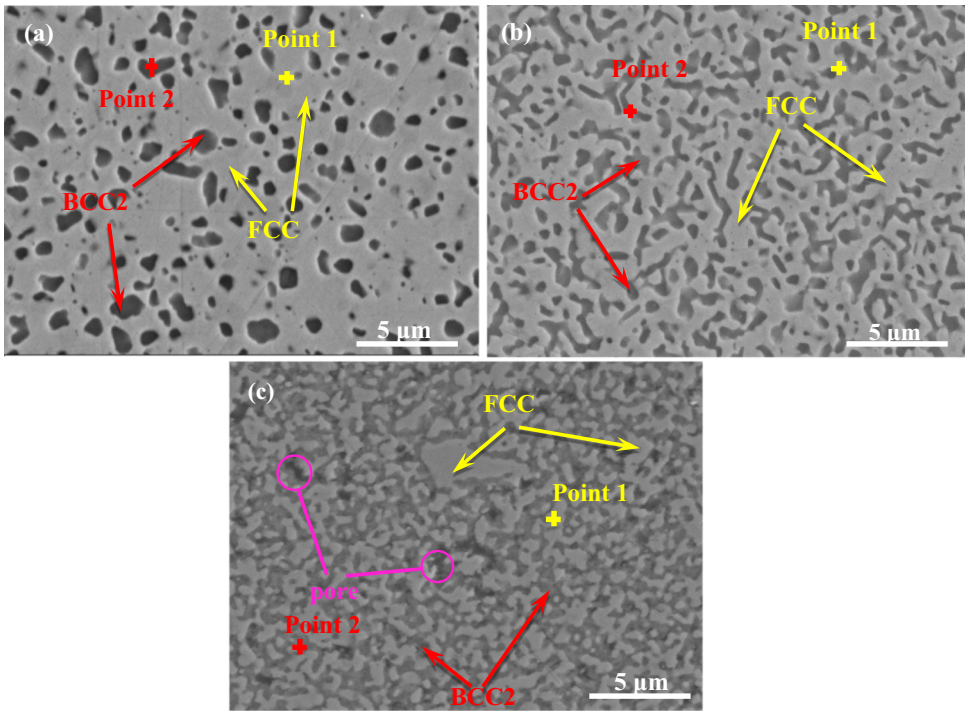

Figure 4 SEM images of Fe–20Mn–6Si–8Cr–5Ni alloy at different milling times: **a** A1, **b** A2, **c** A3.

Table 1 EDS analysis results of Fe–20Mn–6Si–8Cr–5Ni alloy at different milling times (wt%)

Samples	Nominal composition	Fe	Mn	Si	Cr	Ni	C	O
		61	20	6	8	5	–	–
A1	Point1	66.7	15.6	6.4	6.3	5.0	–	–
	Point2	41.1	32.5	13.2	10.4	2.5	–	–
A2	Point1	62.4	19.8	5.5	7.6	4.7	–	–
	Point2	30.6	44.6	18.7	3.9	2.2	–	–
A3	Point1	72.9	1.5	–	8.3	2.5	17.4	–
	Point2	9.1	36.4	9.8	27.8	–	3.9	13.0

96.1%, 98.7% and 94.3%, respectively, and the hardness is 462.7 HV, 527.4 HV and 535.1 HV, respectively. The BCC2 phase is a hard phase that plays a major role in the mechanical properties of the alloy. The higher the content of BCC2, the higher the fracture strength and hardness of the alloy. However, the excessive milling time leads to the appearance of pores in the A3 alloy, which can act as a source of cracks during compression. The initiation and propagation of cracks cause premature failure of the alloy. This phenomenon further confirms that the optimal milling time for Fe–20Mn–6Si–8Cr–5Ni alloy is 50 h.

As can be seen from the SEM of the compressive fracture of the alloy, (as shown in Fig. 7), the milling time has a great influence on the grain size of the alloy. The fracture of the A1 alloy is honeycomb, with dimples (blue circle area) appearing in part of the intergranular fracture plane. The grain size of the A2 alloy is large, and the fracture characteristics are similar to that of the A1 alloy, which belongs to intergranular ductile fracture. The grain size of the A3 alloy is small, and there is no dimple structure in the fracture plane, showing a brittle fracture trend.

Figure 8 shows the stress–strain curves of the A1 and A2 alloys under compression and unloading at room temperature, from which the pre-strain (ε_{pre}), residual strain (ε_r) and SE strain (ε_{se}) of each alloy can be obtained. It is well known that Fe–Mn–Si alloys have shape memory effect, but this memory effect is generated by stress-induced γ-FCC → ε-HCP martensitic transformation and the reverse martensitic transformation induced by heating after unloading. In past studies, Fe–Mn–Si alloys were usually found to have no superelastic properties, but

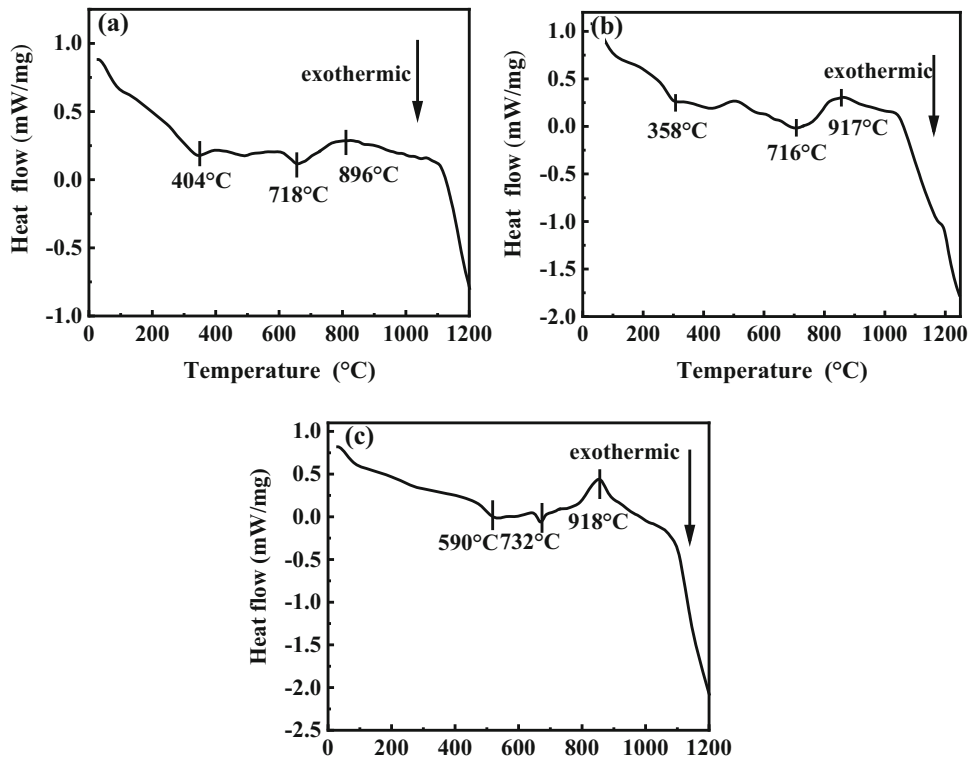

Figure 5 DSC of alloy powder at different milling times: **a** A1, **b** A2; **c** A3.

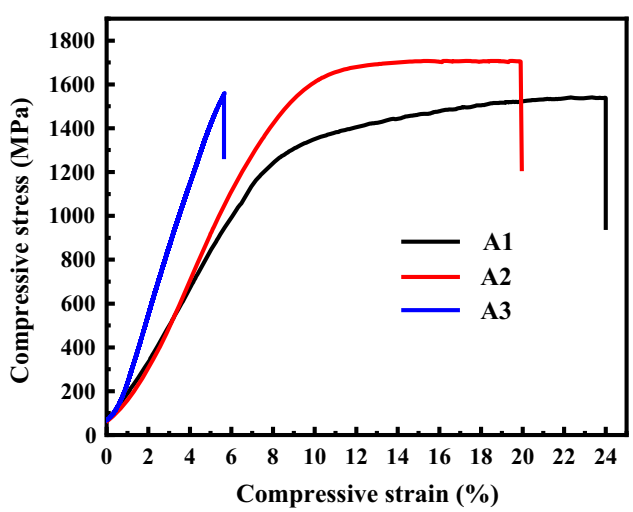

Figure 6 Compressive stress–strain curves of Fe–20Mn–6Si–8Cr–5Ni alloy at room temperature at different milling times.

in this experiment, it was found that Fe–Mn–Si–Cr–Ni alloys prepared with P/M have superelastic properties. The SE strain of the A2 alloy reaches 2.4% at 10% pre-strain and increases to 2.8% as the pre-strain is increased to 15%. On the one hand, A1 alloy samples have low yield strength, which will cause permanent slip and dislocation pileup during plastic deformation, which will hinder the stress-induced formation of the ε-HCP phase [32, 33]. On the other hand, the grain size of the A1 alloy is small, and too fine austenite grains will increase the inhibition effect of grain boundaries on martensite transformation and hinder the nucleation of ε-HCP martensite with single orientation [34]. The above two aspects lead to the lower SE performance of the A1 alloy compared with that of the A2 alloy.

Table 2 Compressive mechanical properties of Fe–20Mn–6Si–8Cr–5Ni alloy at different milling times

Samples	σ_y (MPa)	σ_b (MPa)	Compression strain (%)	Density (%)	Hardness (HV)
A1	1143	1540	24.1	96.1	462.7 ± 4
A2	1326	1753	19.7	98.7	527.4 ± 2
A3	–	1555	5.6	94.3	535.1 ± 4

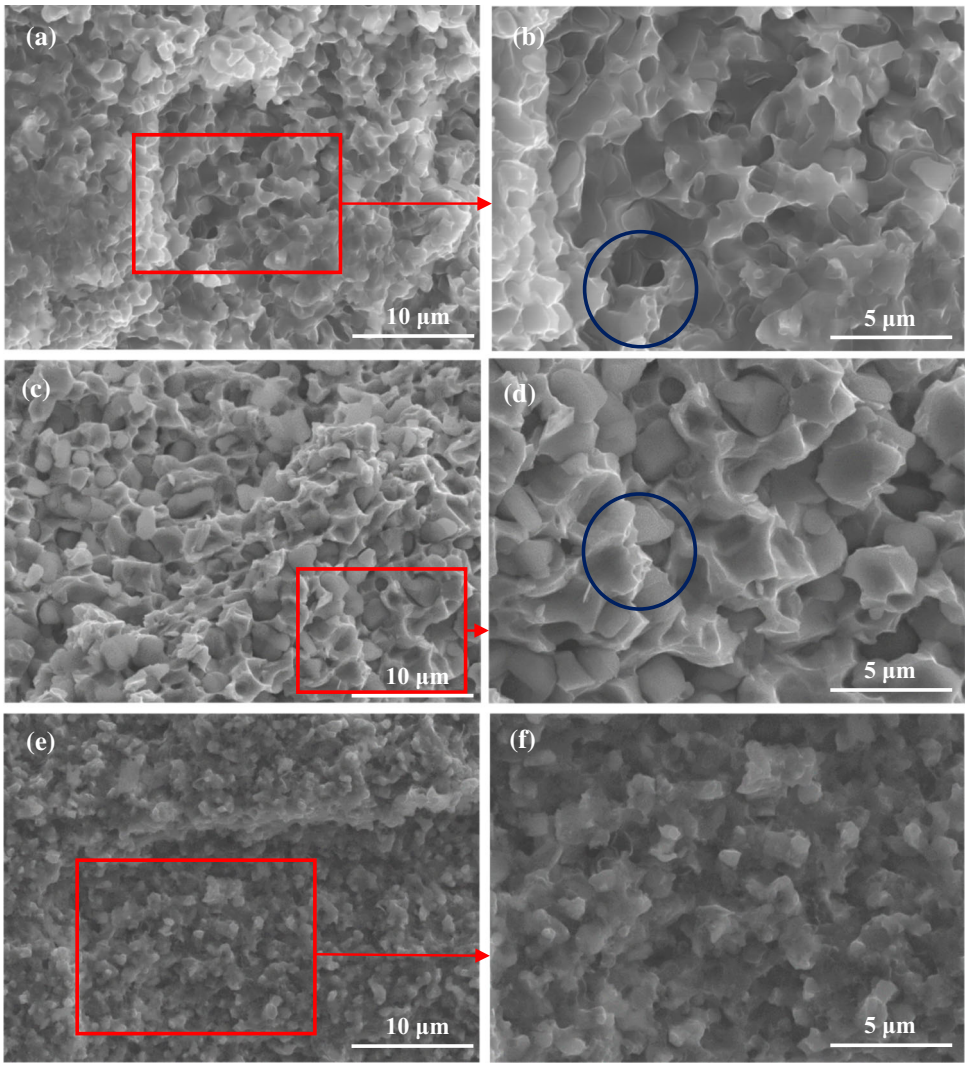

Figure 7 Compression fracture diagrams of the alloy with different milling times: **a**, **b** A1, **c**, **d** A2, **e**, **f** A3.

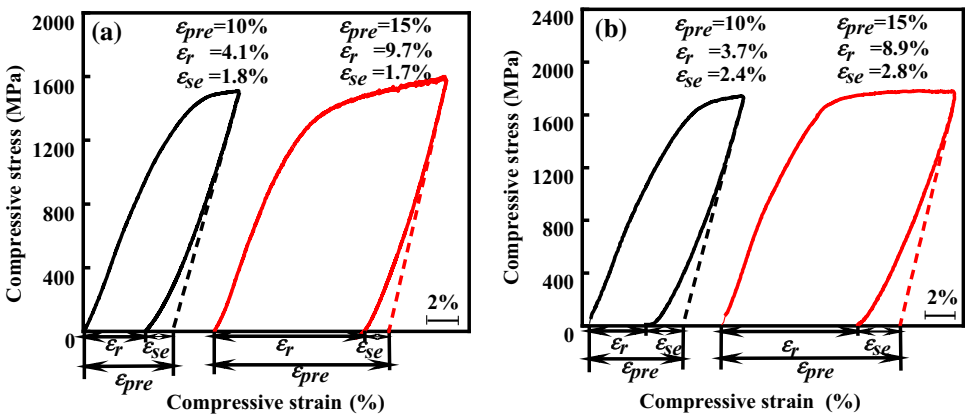

Figure 8 Compressive stress–strain curves of the alloy under 10% and 15% pre-strain: **a** A1, **b** A2.

The static immersion corrosion test results for the A2 alloy sample in both solutions are shown in Fig. 9. It can be seen that after immersion for 240 h, the corrosion rate of the A2 alloy in the HCl solution is faster than that in the NaOH solution, and the rates are 9.625 $g/m^2 \cdot h$ and 0.306 $g/m^2 \cdot h$, respectively. This indicates that the corrosion resistance of Fe–20Mn–6Si–8Cr–5Ni is stronger in the alkaline solution than

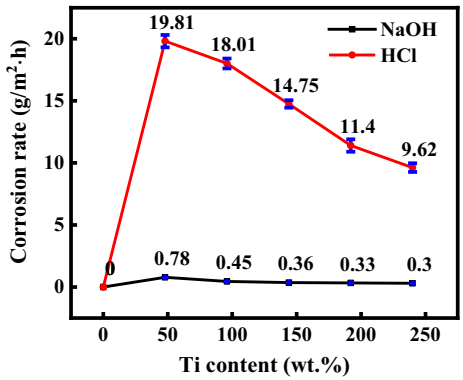

Figure 9 Corrosion rates of the A2 alloy in different corrosion solutions: **a** 3% HCl solution, **b** 20% NaOH.

in the acidic solution. Combining Fig. 10 and Table 3, it can be seen that the A2 alloy produces a structure similar to an oxide film in the NaOH solution, which reduces the corrosion rate. EDS results show that the Fe elements are less abundant in both acidic and alkaline solutions, while Mn, Si and Cr are close to the nominal composition of the FCC phase. This indicates that the BCC2 phase with more Mn, Si and Cr preferentially corrodes, thus exposing the surface of the FCC phase.

Table 3 EDS analysis results of the A2 alloy after corrosion (wt%)

Corrosion solution	Fe	Mn	Si	Cr	Ni	O
HCl	48.64	20.25	7.11	13.06	3.41	7.53
NaOH	58.15	18.28	4.89	9.94	5.38	2.52

Discussion

As the milling time increases, the alloy powder gradually forms a single BCC-saturated solid solution. After the milling time exceeds 50 h, a part of the BCC phase transforms into the HCP phase with low strain energy due to the increase in energy. When the milling time reaches 90 h, the activity of the elements in the alloy powder increases because the energy of the alloy powder is highly concentrated during the long MA process and Fe and Mn are oxidized during the subsequent ramming process. The oxide precipitation reduces the density of the A3 alloy, pores appear inside the A3 alloy (Fig. 4c), and brittle fracture occurs in the compression experiment. In powder metallurgy, density is an important factor affecting the mechanical properties of alloys. The

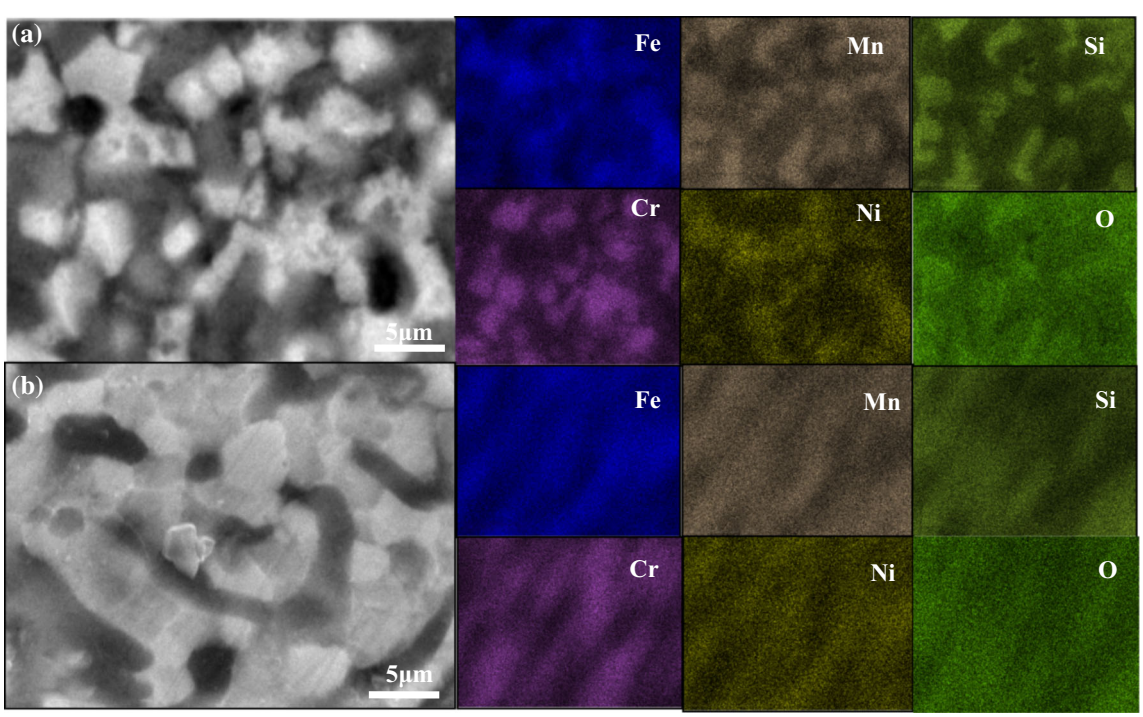

Figure 10 Mapping scan images of the A2 alloy after corrosion with different corrosion solutions: **a** 3% HCl solution, **b** 20% NaOH solution.

density of Fe–28Mn alloy studied by Z.G. Xu [14] and Hodgson [6] was 68.2% and 67.7%, respectively, significantly lower than 98.7% of the A2 alloy, so the fracture strain of the alloy studied by Z.G. Xu was only 11.86%, while the fracture strain of the A2 alloy was up to 20% (Fig. 6). It is also found from the literature that the hardness (130 HV ~ 170 HV, 422.39 HV, 380 HV) of Fe–17Mn–6Si–0.03C [28], Fe–8Cr [35] and Fe–35Mn–5Si [15] alloys prepared by P/M is lower than that of the A2 alloy. It has been confirmed that MA is very necessary for Fe–Mn–Si alloys prepared from P/M.

As the milling time increased, the powder particles gradually became finer (Fig. 1b and Fig. 2), and the fine alloy powder was conducive to the diffusion of elements and phase transition in the sintering process. According to Fig. 1a, a nearly single-phase supersaturated BCC solid solution is obtained after 20–90-h milling, and the DSC (Fig. 5) results indicate that this supersaturated solid solution is metastable. This metastable solid solution undergoes a desolvation or decomposition reaction at about 400 °C, transforming from the BCC phase to the more stable FCC phase. At about 700 °C, Mn- and Si-enriched BCC2 phase is precipitated from the FCC phase. At about 900 °C, the BCC2 phase dissolves during further heating. Combining Fig. 1c and Fig. 4, we find that the BCC2 phase of the alloy increases with increasing milling time. The decomposition temperature of BCC2 in the A2 and A3 alloys is higher than that in the A1 alloy, so BCC2 decomposes more easily in the A1 alloy.

The experimental results show that the effect of BCC2 on the mechanical properties of the alloy is much larger than the effect of fine-grain strengthening. The BCC2 phase is a hard phase [8], and the higher the content of the BCC2 phase, the higher the fracture strength and hardness of the alloy. Interestingly, it is shown experimentally that both A1 and A2 alloys have good superelasticity after 10% and 15% preloading at room temperature. Under external stress, the alloy will generate strain greater than its elastic limit strain, and after stress removal, partial strain will be recovered due to the reverse transformation of martensite into a stable parent phase at the temperature, resulting in superelasticity [36, 37]. The yield strength of the A1 alloy with low BCC2 content is low. Under external forces, the sliding dislocation and Frank–Read source may form entanglements [38], which prevents the Shockley dislocation from moving backward along the original path, hindering the reversion of martensite and reducing the superelasticity of the alloy [32, 33]. At the same time, due to the increase in milling time, the A2 alloy has larger grains, and the larger austenite grains more effectively weaken the inhibitory effect of grain boundaries on martensite transformation and enhance the single-orientation nucleation of ε-HCP martensite [34]. Therefore, the A2 alloy has better SE properties compared with the A1 alloy.

The literature shows that when Fe–Mn alloy is corroded in Cl^- and OH^- solutions, the surface of the alloy is prone to react with oxygen atoms in the air, resulting in Fe_2O_3 and Mn_2O_3, thus improving the corrosion resistance of the alloy [39]. In this work, we find a similar oxide film when the A2 alloy is corroded in NaOH, which results in higher corrosion resistance of A2 in an alkali solution than in an acid solution. EDS analysis of the post-corrosion A2 alloy shows that Mn, Si and Cr are close to the nominal composition, so we conjecture that the BCC2 phase in the A2 alloy is preferentially corroded, thus showing the FCC phase grains. The reason may be that FCC is a tightly bound lattice with a higher filling rate than BCC2, which makes it have better corrosion resistance [40].

Conclusions

In this paper, the effect of milling time on the organization and mechanical properties of Fe–20Mn–6Si–8Cr–5Ni alloy was investigated. With the increase in milling time, the powder particles gradually become finer (Fig. 1b and Fig. 2), which is beneficial to the diffusion of elements and phase transformation during the sintering process. The sintered alloy is mainly composed of FCC and BCC2 phases. The amount of BCC2 precipitates increases with the increase in milling time, and the higher the content of BCC2 phase, the higher the fracture strength, yield strength and hardness of the alloy.

The presence of pores in the A3 alloy makes it brittle fracture, so among these three alloys, the A2 alloy has the highest yield and fracture strengths of 1326 MPa and 1753 MPa, respectively. The increase in BCC2 content increases the yield strength of the A2 alloy, and the sliding dislocations and Frank–Read sources are less likely to become entangled when external forces are applied, which promotes the

inverse transformation of martensite and improves A2 alloy superelasticity. The superelasticity strain of the A2 alloy can reach 2.8%. When corroding in NaOH solution, the surface of the A2 alloy is easy to produce oxide film, which makes the corrosion resistance of the A2 alloy in the NaOH solution higher than that in the HCl solution.

Acknowledgements

This work was supported by the Youth Talent Support Program of Danyang City of Jiangsu Province of China (Grant number: 2019003) and the Key Scientific Research Projects of Hebei Province Colleges and Universities of China (ZD2021099).

Data availability

Data and code availability: The raw/processed data required to reproduce these findings cannot be shared at this time as the data also form part of an ongoing study.

Declarations

Conflict of interest The authors declare that they have no known competing financial interests or personal relationships that could have appeared to influence the work reported in this paper.

Ethical approval This paper does not involve experiments on ethical issues.

References

[1] Yoshinaka F, Sawaguchi T, Takamori S, Emura S (2022) Transformation-induced plasticity via $\gamma \rightarrow \varepsilon \rightarrow \alpha'$ and $\gamma \rightarrow \varepsilon \rightarrow \gamma$ martensitic transformations in Fe-15Mn-10Cr-8Ni-4Si alloy. Mater Sci Eng A 833:142583. https://doi.org/10.1016/j.msea.2021.142583

[2] Esquivel I, Malarría J (2021) Design, manufacturing, and performance of Fe-Mn-Si-Ni-Cr shape memory seamless couplings. Adv. Ind. Manuf. Eng. 3:100061. https://doi.org/10.1016/j.aime.2021.100061

[3] Hong KN, Yeon YM, Shim WB, Kim DH (2020) Recovery behavior of Fe-based shape memory alloys under different restraints. Appl Sci 10:3441. https://doi.org/10.3390/app10103441

[4] Choi S, Choi E, Kim WJ (2021) Austenite grain size effect on recovery stress and recovery strain of Fe-Mn-Si-Cr-Ni-001C alloy severely plastically deformed by differential speed rolling. Mater Charact 175:111097. https://doi.org/10.1016/j.matchar.2021.111097

[5] Collazo A, Figueroa R, Mariño-Martínez C (2021) Microstructure and thermomechanical characterization of Fe-28Mn-6Si-5Cr shape memory alloy. Metals 11:649. https://doi.org/10.3390/met11040649

[6] Xu ZG, Hodgson MA, Cao P (2015) A comparative study of powder metallurgical (PM) and wrought Fe-Mn-Si alloys. Mater Sci Eng A 630:116124. https://doi.org/10.1016/j.msea.2015.02.021

[7] Arora A, Mula S (2022) Phase evolution characteristics, thermal stability, and strengthening processes of Fe -Ni based ODS invar steel produced by mechanical alloying and spark plasma sintering. Mater Sci Eng A 856:143972. https://doi.org/10.1016/j.msea.2022.143972

[8] Pricop B, Borza F, Ozkal B (2021) Influence of thermal and mechanical/powder processing on microstructure and dynamic stiffness of Fe-Mn-Si-Cr-Ni shape memory alloy. T Indian Metals 74:1409–1418. https://doi.org/10.1007/s12666-021-02215-8

[9] Wang GF, Jia ZL, Jing T (2022) Effect of sintering time on the structural and magnetocaloric properties of Mn-Fe-P-Si-Ge-B alloys prepared by spark plasma sintering. J Alloys Compd 925:166–365. https://doi.org/10.1016/j.jallcom.2022.166365

[10] Goudarzi P, Moazami-Goudarzi M, Masoudi A (2022) Sintering, microstructure and properties of absorbable Fe-Mn-xCu alloys. Mater Chem Phys 387:126–368. https://doi.org/10.1016/j.matchemphys.2022.126368

[11] Suntharavel Muthaiah VM, Koch CC, Mula S (2021) Thermal stability and mechanical properties of Fe-Cr-Zr alloys developed by mechanical alloying followed by spark plasma sintering. J Alloys Compd 856:158–266. https://doi.org/10.1016/j.jallcom.2020.158266

[12] Zhou X, Liu Y, Yu L, Ma Z, Guo Q, Huang Y, Li H (2017) Microstructure characteristic and mechanical property of transformable 9Cr-ODS steel fabricated by spark plasma sintering. Mater Des 132:158–169. https://doi.org/10.1016/j.matdes.2017.06.063

[13] Arabi-Hashemi A, Lee WJ, Leinenbach C (2018) Recovery stress formation in FeMnSi based shape memory alloys: impact of precipitates, texture and grain size. Mater Des 139:258–268. https://doi.org/10.1016/j.matdes.2017.11.006

[14] Xu ZG, Hodgson MA, Cao P (2016) Effects of mechanical milling and sintering temperature on the densification, microstructure and tensile properties of the Fe-Mn-Si powder

compacts. J Mater Sci Technol 32(11):1161–1170. https://doi.org/10.1016/j.jmst.2016.08.024

[15] Torkan S, Ataie A, Abdizadeh H, Sheibani S (2014) Effect of milling energy on preparation of nano-structured Fe70Si30 alloys. Powder Technol 267:145–152. https://doi.org/10.1016/j.powtec.2014.07.020

[16] Hasnaoui N, Hafs A, Hafs T, Bendjeda F (2022) Structural, microstructural characterisation and magnetic properties of nanocrystalline Fe-10 wt% Pb alloy powders synthesised by mechanical alloying process. J Alloys Compd 899:163–338. https://doi.org/10.1016/j.jallcom.2021.163338

[17] Zeraati M, Arshadizadeh R, Chauhan NPS, Sargazi G (2021) Genetic algorithm optimization of magnetic properties of Fe-Co-Ni nanostructure alloys prepared by the mechanical alloying by using multi-objective artificial neural networks for the core of transformer. Mater Today Commun 28:102–653. https://doi.org/10.1016/j.mtcomm.2021.102653

[18] Haušild P, Čech J, Bouček V, Karlík M (2019) Mechanical alloying of Fe-Al-Si intermetallic compounds using pure and pre-alloyed powders. Procedia Struct Integrity 23:179–184. https://doi.org/10.1016/j.prostr.2020.01.083

[19] Toroghinejad MR, Pirmoradian H, Shabani A (2020) Synthesis of FeCrCoNiCu high entropy alloy through mechanical alloying and spark plasma sintering processes. Mater Chem Phys 289:126433. https://doi.org/10.1016/j.matchemphys.2022.126433

[20] Shyni P, Perumal A (2015) Structural and magnetic properties of nanocrystalline Fe-Co-Si alloy powders produced by mechanical alloying. J Alloys Compd 648:658–666. https://doi.org/10.1016/j.jallcom.2015.06.237

[21] Mariño-Gámez AE, Guillermo-E Acosta-González MI, Pech-Canul (2022) Influence of high energy ball milling on structural, microstructural and optical properties of TiO2 nanoparticles. Ceram Int 48:3362–3367. https://doi.org/10.1016/j.ceramint.2021.10.111

[22] Adelfar R, Mirzadeh H, Ataie A, Malekan M (2020) Crystallization kinetics of mechanically alloyed amorphous Fe-Ti alloys during annealing. Adv Powder Technol 31:3215–3221. https://doi.org/10.1016/j.apt.2020.06.006

[23] Saito T, Kapusta Cz, Takasaki A (2014) Synthesis and characterization of Fe-Mn-Si shape memory alloy by mechanical alloying and subsequent sintering. Mater Sci Eng A 592:88–94. https://doi.org/10.1016/j.msea.2013.10.097

[24] Bazzi K, Meka VM, Rathi A, Jayaraman TV (2019) Influence of temperature on the magnetic properties of nanostructured Fe-49 wt.% Co-2 wt.% V alloy powder synthesized by mechanically milling pre-alloyed gas-atomized powder. Mater Chem Phys 277:36–46. https://doi.org/10.1016/j.matchemphys.2019.01.044

[25] Zhou XS, Dong HK, Wang YS, Yuan MN (2022) Microstructure characteristics and mechanical performance of Fe-Cr-Ni-Al-Ti superalloy fabricated by powder metallurgy. J Alloys Compd 918:165612. https://doi.org/10.1016/j.jallcom.2022.165612

[26] Zhao KX, Zhang ZR, Li S, Tang Y (2022) The forming mechanism and thermal stability of W-Zr super-saturated solid solution powder prepared by mechanical alloying. J Alloys Compd 920:165–928. https://doi.org/10.1016/j.jallcom.2022.165928

[27] Spandana D, Desai H, Chakravarty D (2020) Fabrication of a biodegradable Fe-Mn-Si alloy by field assisted sintering. Adv powder Technol 31:4577–4584. https://doi.org/10.1016/j.apt.2020.10.012

[28] Xu F, Zhang Z, Shen B (2010) Preparation of iron-based shape memory alloys by powder metallurgy. Sci Technol Innov Herald 2010(1):58–58. https://doi.org/10.16660/j.cnki.1674-098x.2010.01.116

[29] Q. Zou, X.H. Ye, Y.G. Li, Effects of Ti on microstructure and properties of Fe-Mn-Si-Cr-Ni shape memory alloy, Mater. Chem. Phys. 293 (2023) 126992. https://doi.org/10.1016/j.matchemphys.2022.126992

[30] Peng H, Hua J, Xu B, Wen Y (2019) Fabrication of ferrite-coated magnetic Fe-Mn-Si-Cr-Ni alloy utilizing selective oxidation of Mn element. IEEE T Magn 55:2900307. https://doi.org/10.1109/TMAG.2019.2904568

[31] Malafaia AM, Nascimento VR, Sousa LM (2019) Anomalous cyclic oxidation behaviour of a Fe-Mn-Si-Cr-Ni alloy-a finite element analysis. Corros Sci 147:223–230. https://doi.org/10.1016/j.corsci.2018.11.018

[32] Sawaguchi T, Maruyama T, Otsuka H (2016) Design concept and applications of Fe-Mn-Si based alloys from shape-memory to seismic response control. Mater Trans 57:283–293. https://doi.org/10.2320/matertrans.MB201510

[33] Malamud F, Guerrero LM, Roca PL (2018) Role of Mn and Cr on structural parameters and strain energy during FCC-HCP martensitic transformation in Fe-Mn-Cr shape memory alloys. Mater Des 139:314–323. https://doi.org/10.1016/j.matdes.2017.11.017

[34] Peng HB, Wang G, Wang S (2018) Key criterion for achieving giant recovery strains in polycrystalline Fe-Mn-Si based shape memory alloys. Mater Sci Eng A 712:37–49. https://doi.org/10.1016/j.msea.2017.11.071

[35] Z.W. Jin, Y.N. Huang, Y.C. Wu, Microstructure characterization of Fe-(8/15) Cr alloy fabricated by mechanical alloying and spark plasma sintering, T. Mater. Heat. Treat. 41 (2020) 72–79. https://doi.org/10.13289/j.issn.1009-6264.2020-0178

[36] Baruj A, Bertolino G, Troiani HE (2010) Temperature dependence of critical stress and pseudoelasticity in a Fe-

Mn-Si-Cr pre-rolled alloy. J Alloys Compd 502:54–58. https://doi.org/10.1016/j.jallcom.2010.04.123

[37] Mohri M, Ferretto I, Leinenbach C (2022) Effect of thermomechanical treatment and microstructure on pseudoelastic behavior of Fe-Mn-Si-Cr-Ni-(V, C) shape memory alloy. Mater Sci Eng A 855:143917. https://doi.org/10.1016/j.msea.2022.143917

[38] Druker A, Vermaut P, Malarría J (2018) The shape recovery conditions for Fe-Mn-Si alloys: an interplay between martensitic transformation and plasticity. Mater Charact 139:319–327. https://doi.org/10.1016/j.matchar.2018.03.018

[39] Han Y, Kong FL, Han FF (2016) New Fe-based soft magnetic amorphous alloys with high saturation magnetization and good corrosion resistance for dust core application. Intermetallics 76:18–25. https://doi.org/10.1016/j.intermet.2016.05.011

[40] Parakh A, Vaidya M, Kumar N, Chetty R (2021) Effect of crystal structure and grain size on corrosion properties of AlCoCrFeNi high entropy alloy. J Alloys Compd 863:158056. https://doi.org/10.1016/j.jallcom.2020.158056

Publisher's Note Springer Nature remains neutral with regard to jurisdictional claims in published maps and institutional affiliations.

Springer Nature or its licensor (e.g. a society or other partner) holds exclusive rights to this article under a publishing agreement with the author(s) or other rightsholder(s); author self-archiving of the accepted manuscript version of this article is solely governed by the terms of such publishing agreement and applicable law.